W.G. Yang et al., Journal of Alloys and Compounds, 902 (2022) 163722
https://doi.org/10.1016/j.jallcom.2022.163722

Ternary V_{ss}–V_3Si–V_5SiB_2 eutectic formation in the V–Si–B system

W.G. Yang[1], G. Hasemann[2], M. Yazlak[3], B. Gorr[4], R. Schwaiger[1,5], M. Krüger[2,*]

[1] *Forschungszentrum Jülich GmbH, Institute of Energy and Climate Research, Microstructure and Properties of Materials (IEK−2), Leo-Brand-Str.1, 52425, Jülich, Germany*

[2] *Otto-von-Guericke University Magdeburg, Institute of Materials and Joining Technology, Universitätsplatz 2, 39106, Magdeburg, Germany*

[3] *University Siegen, Institute of Materials Technology, Paul-Bonatz-Strasse 9-11, 57076, Siegen, Germany*

[4] *Karlsruhe Institute of Technology, Institute for Applied Materials – Applied Materials Physics (IAM−AWP), Hermann-von-Helmholtz-Platz 1, 76344, Eggenstein-Leopoldshafen, Germany*

[5] *Chair of Energy Engineering Materials, Faculty 5, RWTH Aachen University, Templergraben 55, 52056, Aachen, Germany*

Highlights

- The composition of the ternary V_{ss}–V_3Si–V_5SiB_2 eutectic reaction was determined.
- The liquidus projection surrounding the ternary eutectic reaction was carefully investigated experimentally.
- Competitive solidification behavior between V_{ss}–V_5SiB_2 and V_{ss}–V_3Si–V_5SiB_2 eutectics was observed depending on cooling.
- The competitive formation of the two eutectics was discussed employing the Jackson-Hunt theory.

Abstract

The solidification behavior close to the ternary V_{ss}–V_3Si–V_5SiB_2 eutectic reaction in the V–Si–B system has been experimentally investigated via arc-melting. According to the microstructure investigation, which is performed by SEM observations, EDS and EBSD measurements and XRD analysis, the composition of the ternary eutectic reaction has been determined at V−9Si−6.5B (at.%). Its microstructures in two different sample sections with different cooling rates were further investigated and compared with the calculated result of the developed eutectic growth theory based on the Jackson-Hunt model to reveal the competitive solidification behavior between the two-phase V_{ss}–V_5SiB_2 and three-phase V_{ss}–V_3Si–V_5SiB_2 eutectic growth. As a result, the liquidus projection around the ternary eutectic reaction was modified and the cross section of the ternary V_{ss}–V_3Si–V_5SiB_2 eutectic coupled zone along the monovariant V_{ss}–V_5SiB_2 and V_3Si–V_5SiB_2 reaction lines was schematically proposed.

Keywords

high-temperature alloys; intermetallics; microstructure; metallography; scanning electron microscopy, SEM; X-ray diffraction

*E-mail address: manja.krueger@ovgu.de

1. Introduction

Most high-temperature properties, e.g. high-temperature strength and creep resistance, are correlating with the high melting temperature. Thus, refractory metals have been used to design alloys for high-temperature structural applications in different ways. They have been micro-/macro-alloyed with other elements to design refractory metal-based alloys, for example molybdenum- [1–3], niobium- [4,5] and vanadium-based alloys [6]. Alternatively, refractory metals are used as alloying elements, for example in Ni-based superalloys [7]. Furthermore, considering the cocktail effect [8,9], refractory metals are also alloying elements in high-entropy alloys (HEAs) for high-temperature applications, e.g. high-entropy superalloys (HESAs) [10], refractory high-entropy alloys (RHEAs) [11] and eutectic high-entropy alloys (EHEAs) [12,13].

The three-phase V_{ss}–V_3Si–V_5SiB_2 alloys are a class of vanadium-based alloys. This alloy design is inspired by the three-phase Mo_{ss}–Mo_3Si–Mo_5SiB_2 alloys [1], which are attractive because of their excellent creep resistance provided by the hard intermetallic phases (Mo_3Si and Mo_5SiB_2) and the improved high-temperature oxidation resistance resulting from a protective borosilicate layer covering the alloy surface [3]. In the same way, the intermetallic phases V_3Si and V_5SiB_2 can be expected to improve the creep resistance and high-temperature oxidation resistance of the vanadium alloy. To finely distribute the intermetallic phases in the solid solution phase, Krüger et al. [14–17] produced a three-phase V_{ss}–V_3Si–V_5SiB_2 V–9Si–13B alloy (if not state otherwise, all concentrations are given in at.%) using powder metallurgy (PM) based on the isothermal section of the V–Si–B system at 1600 °C reported by Nunes et al. [18]. PM V–9Si–13B showed a high-temperature compressive strength comparable to the strength of Ni-based superalloy CMSX-4 up to 900 °C [14,19] and creep resistance comparable to a cobalt-nickel superalloy at 900 °C [16,20]. Regardless of the improved oxidation resistance of PM V–9Si–13B [14] compared to the V–5Cr–5Ti alloy [21] at 600 °C, the oxidation resistance of PM V–9Si–13B still needs to be further improved compared to the CMSX-4 [14,21].

To produce the three-phase V_{ss}–V_3Si–V_5SiB_2 alloys via a casting process, a precisely determined liquidus projection would be useful for the choice of alloy compositions. Recently, a systematic investigation on the liquidus projection in the vanadium-rich region of the V–Si–B system was carried out by Hasemann [22] via arc-melting to re-evaluate the thermodynamically calculated liquidus projection by Pinto da Silva et al. [23]. Five specific primary solidification areas (V_{ss}, V_3Si, V_5SiB_2, V_3B_2, VB) were

confirmed in the three-phase V_{ss}–V_3Si–V_5SiB_2 field proposed by Nunes et al. [18], as shown in Fig. 1 (a). The three-phase V_{ss}–V_3Si–V_5SiB_2 alloys were produced within the V_{ss}–, V_3Si– and V_5SiB_2–primary solidification areas [22]. Furthermore, Hasemann [22] proposed two invariant reactions in the vanadium-rich corner of the V–Si–B system:

$$L \leftrightarrow V_{ss} + V_5SiB_2 + V_3Si \quad (E_t)$$

$$L + V_3B_2 \leftrightarrow V_{ss} + V_5SiB_2 \quad (U)$$

However, different invariant reactions were proposed previously by other researchers, as shown in Fig. 1 (b).

In the thermodynamically calculated liquidus projection by Pinto da Silva et al. [23], the reaction (E_t) has also been reported, however, instead of the reaction (U) another invariant reaction was described:

$$L \leftrightarrow V_{ss} + V_5SiB_2 + V_3B_2 \quad (E')$$

The origin of this difference may be caused by the limited accuracy of the thermodynamical calculation due to almost identical calculated temperatures of the reactions (E_t) and (E'). By contrast, de Lima et al. [24] reported the reaction (U), while another invariant reaction, (U'), instead of the reaction (E_t) was described according to the microstructures observed:

$$L + V_3Si \leftrightarrow V_{ss} + V_5SiB_2 \quad (U')$$

The formation of the two-phase V_{ss}–V_5SiB_2 microstructure was observed after the two-phase V_{ss}–V_3Si and two-phase V_3Si–V_5SiB_2 formation [24]. This phenomenon was confirmed by Hasemann [22], however, the three-phase V_{ss}–V_3Si–V_5SiB_2 eutectic microstructure was also observed in some alloys located within the V_{ss}–primary solidification area or the V_5SiB_2–primary solidification area [22]. Therefore, it is reasonable that in the present work the reactions (E_t) and (U) proposed by Hasemann [22] are adopted.

The eutectic reaction (E_t) is the theoretical base to produce the ternary V_{ss}–V_3Si–V_5SiB_2 eutectic alloy. Due to the absence of a primary phase, the ternary V_{ss}–V_3Si–V_5SiB_2 eutectic alloy would be expected to have improved mechanical properties, especially in terms of strength, compared to other three-phase alloys with a primary phase. To the best of our knowledge, until now the exact ternary eutectic alloy composition has not yet been reported. Thus, the first aim of the present work is to determine this composition via arc-melting experiments. Furthermore, the two-phase V_{ss}–V_5SiB_2 formation after the two-phase V_{ss}–V_3Si or two-phase V_3Si–V_5SiB_2 formation, which has been found by de Lima et al. [24], can be attributed to

undercooling effects. Thus, the ternary eutectic alloy found by this work was used to qualitatively investigate the influence of undercooling on the solidification behavior. Its microstructures in two different sample sections that had experienced different undercoolings were observed and compared. In this way, a competitive solidification behavior between the two-phase V_{ss}–V_5SiB_2 and the three-phase V_{ss}–V_3Si–V_5SiB_2 eutectic formation has been found. To reveal this competitive solidification behavior, both types of eutectic growth were simplified to the lamellar eutectic growth and then the developed Jackson-Hunt theory [25] was applied, which was reconsidered in this work by a series of additional assumptions for the irregular lamellar eutectic growth at high undercoolings.

(a)

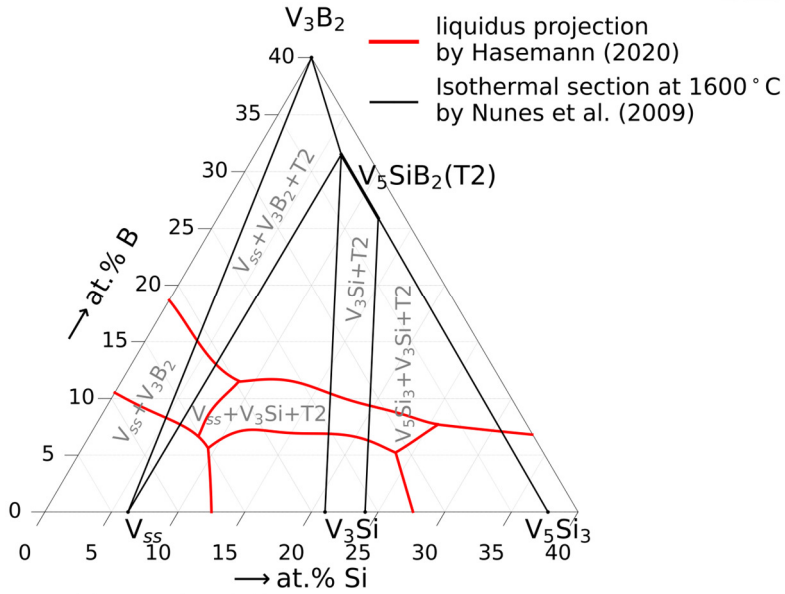

(b)

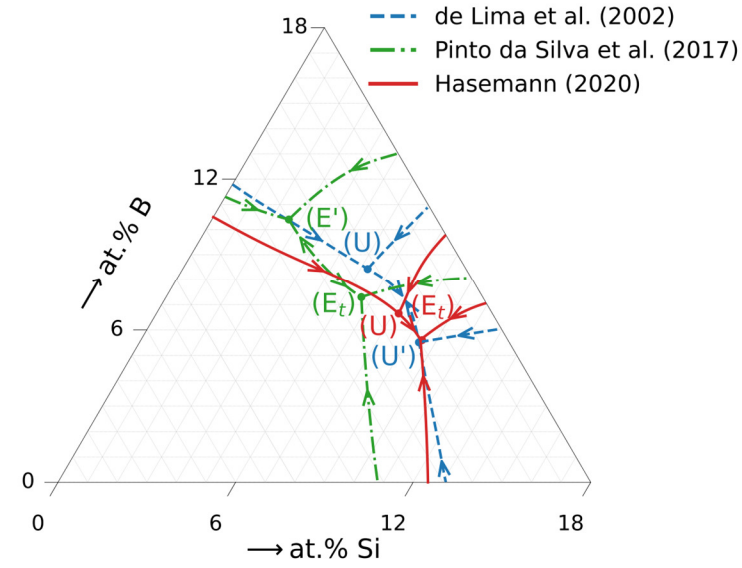

Fig. 1. (a) Overlapping the isothermal section of the V–Si–B system at 1600 °C presented by Nunes et al. [18] and the liquidus projection proposed by Hasemann [22] via arc-melting; (b) comparing different liquidus projections in the vanadium-rich corner of the V–Si–B system (> 82 at.% V) [22–24].

2. Experimental

2.1. Sample preparation and characterization

V–Si–B alloys were produced by conventional arc-melting under argon atmosphere. According to the nominal compositions of alloys listed in Table 1, the raw materials for arc-melting were carefully weighed in the form of high-purity elemental turnings of V (99.7 wt.%) and granules of Si (99.99 wt.%) and B (99.0 wt.%) to produce a 15 g sample for each alloy investigated. Each button was remelted and flipped five times to ensure a homogenous compositional distribution of all elements. A weight loss of < 1% indicates that the compositions after arc-melting are very close to the nominal composition. For confirmation, the chemical compositions listed in Table 1 were measured by inductively coupled plasma optical emission spectroscopy (ICP-OES, iCAP 7600, Thermo Fisher Scientific, USA). For metallographic preparation, the samples were embedded in a cold mounting resin (Expoy 2000, Cloeren Technology, Wegberg, Germany), subsequently ground down to 2000 grit using SiC paper, polished with 15 μm, 6 μm, 3 μm and 1 μm diamond suspension, and finished by polishing with colloidal silica.

Table 1. Nominal and chemical compositions of alloys produced in this work

Alloy #	Nominal composition [at.%]	Chemical composition [at.%]
1	V–9Si–5.5B	V–8.9Si–5.4B
2	V–9Si–6B	V–8.9Si–6.0B
3	V–9Si–6.5B	V–8.8Si–6.5B
4	V–9Si–7B	V–8.4Si–7.1B
5	V–8Si–6.5B	V–8.3Si–6.5B
6	V–8.5Si–6.5B	V–8.5Si–6.1B
7	V–9.5Si–6.5B	V–9.4Si–6.3B
8	V–10Si–6.5B	V–9.8Si–6.6B
9	V–8.5Si–7B	V–8.9Si–6.8B
10	V–9.5Si–6B	V–9.7Si–5.7B

A Zeiss Merlin (Zeiss Microscopy, Oberkochen, Germany) scanning electron microscope (SEM) was used to observe the microstructures using the secondary electron (SE) and the backscatter electron (BSE) mode. Energy-dispersive X-ray spectroscopy (EDS, X-Max 150, Oxford Instruments, UK) was performed to check the composition of each phase. Furthermore, electron backscatter diffraction (EBSD, Oxford Instruments, UK) with a scanning step size smaller than 0.25 μm was used to identify the phases and obtain the phase maps. The polished bulk samples were directly used to perform X-ray diffraction (XRD) at room temperature using a

diffractometer EMPYREAN (Malvern Panalytical, UK) and a diffractometer D8 ADVANCE (Bruker, USA) to identify the crystal structures of the phases. The lattice parameters of the phases were determined using the software GSAS-II [26] applying the Pawley refinement [27], where the intensities of diffraction peaks are variable.

2.2. Application of the eutectic growth theory

To study the competitive solidification behavior between the two-phase V_{ss}–V_5SiB_2 and three-phase V_{ss}–V_3Si–V_5SiB_2 eutectic growth in alloy V–9Si–6.5B (#3), both eutectic growth modes are simplified to the lamellar eutectic growth. An analytical model has been developed based on the theory proposed by Jackson and Hunt [25] to describe the steady-state irregular lamellar eutectic growth at high undercoolings in a ternary system.

According to Jackson and Hunt [25] the undercooling needed for the eutectic growth consists of three parts:

$$\Delta T = \Delta T_c + \Delta T_\sigma + \Delta T_k \quad (1)$$

where ΔT_c is the constitutional undercooling due to the difference of composition at the liquid-solid interface compared to the eutectic composition, ΔT_σ is the capillary undercooling due to the non-planar liquid-solid interface and ΔT_k represents the kinetic undercooling, which is negligible in most metallic eutectic systems compared to the other two contributions, due to the change of the chemical potential driving atoms attached to the liquid-solid interface [25].

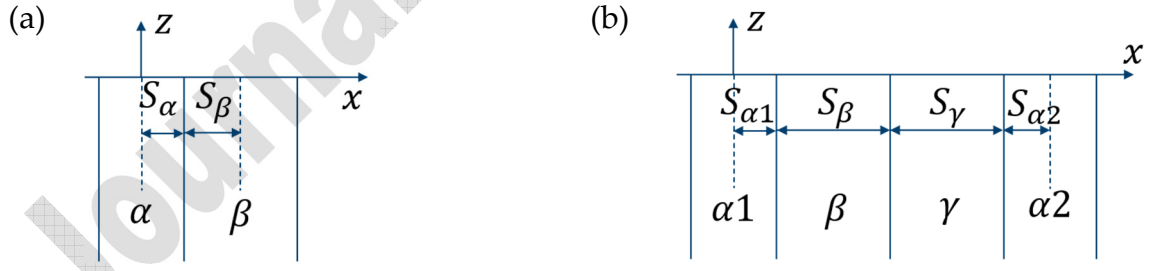

Fig. 2. Schematic of the assumed planar liquid-solid interface for (a) the two-phase eutectic growth and (b) the three-phase eutectic growth

To calculate ΔT_c, following the Jackson-Hunt theory [25], a planar liquid-solid interface is assumed to describe the solute diffusion of two-phase eutectic growth as shown in Fig. 2 (a), where z-direction is the solidification direction and $S_{\alpha/\beta}$ is half the width of each phase. For the irregular eutectic growth, Magnin and Kurz [28] have evaluated this assumption and found that it is valid for high growth velocities. Thus, the composition of element i at the position (x, z), $C_i(x, z)$, can be calculated as follows:

$$C_i(x,z) = C_{i0} + B_{i0}\mathrm{e}^{-\frac{v}{D_i}z} + \sum_{n=1}^{\infty} B_{in}\cos\left(\frac{n\pi x}{S_\alpha + S_\beta}\right)\mathrm{e}^{\left(-\frac{v}{2D_i}-\sqrt{\left(\frac{v}{2D_i}\right)^2+\left(\frac{n\pi}{S_\alpha+S_\beta}\right)^2}\right)z} \quad (2)$$

where C_{i0} is the initial composition of element i, v is the growth velocity, D_i is the diffusion coefficient of element i, B_{i0} and B_{in} are 0-th and n-th Fourier series coefficients respectively. Here, the number of used Fourier series coefficients is 100 instead of infinite. There are three boundary conditions for this solution. The first two boundary conditions can originally be satisfied by the solution function:

$$C_i(x,z) = C_{i0} \text{ at } z = \infty \quad (3)$$

$$\frac{\partial C_i(x,z)}{\partial z} = 0 \quad \text{at } x = 0 \text{ and } x = S_\alpha + S_\beta \quad (4)$$

The third boundary condition is to keep the mass of solute transfer at the interface constant:

$$\begin{cases} \left(\frac{\partial C_i(x,z)}{\partial z}\right)_{z=0} = \frac{v\cdot(C_{i\alpha}-C_{i0})}{D_i} & 0 \le x \le S_\alpha \\ \left(\frac{\partial C_i(x,z)}{\partial z}\right)_{z=0} = \frac{v\cdot(C_{i\beta}-C_{i0})}{D_i} & S_\alpha \le x \le S_\beta \end{cases} \quad (5)$$

To expand the Jackson-Hunt model to large undercoolings, Trivedi et al. [29] have studied two types of binary eutectic phase diagrams, the so-called "cigar-shaped" phase diagram, where the liquidus and solidus lines are parallel below the eutectic temperature, and the phase diagram, where the solute distribution coefficient between liquid and solid phases is constant below the eutectic temperature. In this work, the "cigar-shaped" phase diagram below the eutectic temperature was used to consider the change of solute distribution coefficients depending on the temperature. Thus, although the third boundary condition has the same form as proposed by Jackson and Hunt [25], it has a different meaning for the solute distributions. By satisfying the third boundary condition the constants B_{i0} and B_{in} can be determined:

$$B_{i0} = -\frac{(C_{i\alpha}-C_{i0})\cdot S_\alpha + (C_{i\beta}-C_{i0})\cdot S_\beta}{S_\alpha + S_\beta} \quad (6)$$

$$B_{in} = -\frac{2}{F_n}\cdot\frac{1}{n\pi}\cdot\frac{v}{D_i}\cdot\sin\left(\frac{n\pi\cdot S_\alpha}{S_\alpha+S_\beta}\right)\cdot(C_{i\beta}-C_{i\alpha}) \quad (7)$$

where, F_n is defined in the following to simplify Eq. (7):

$$F_n = \frac{1}{2}\left[1+\sqrt{1+\left(\frac{n\pi}{S_\alpha+S_\beta}\cdot\frac{2D_i}{v}\right)^2}\right] \quad (8)$$

Similarly, a planar liquid-solid interface is assumed to describe the solute diffusion of three-phase eutectic growth as shown in Fig. 2 (b). In contrast to the planar interface of two-phase eutectic growth, where $S_\alpha + S_\beta = \frac{\lambda}{2}$, the planar interface of three-phase eutectic growth is described as: $S_{\alpha 1} + S_\beta + S_\gamma + S_{\alpha 2} = \lambda$, in which $S_{\alpha 1/\alpha 2}$ is the half width of the solid solution phase and $S_{\beta/\gamma}$ is the width of the intermetallic phases. Splitting the α-phase into two parts can obtain the phase sequence of $\alpha\beta\gamma\alpha\gamma\beta\alpha$, where each phase is in contact with the other two phases. The solution of the solute diffusion for this three-phase eutectic growth can be obtained in the same way as for the two-phase eutectic growth:

$$C_i(x,z) = C_{i0} + B_{i0}\mathrm{e}^{-\frac{v}{D_i}z} + \sum_{n=1}^{\infty} B_{in}\cos\left(\frac{n\pi x}{S_\alpha + S_\beta + S_\gamma}\right)\mathrm{e}^{\left(-\frac{v}{2D_i} - \sqrt{\left(\frac{v}{2D_i}\right)^2 + \left(\frac{n\pi}{S_\alpha + S_\beta + S_\gamma}\right)^2}\right)z} \tag{9}$$

$$B_{i0} = -\frac{(C_{i\alpha} - C_{i0})S_\alpha + (C_{i\beta} - C_{i0})S_\beta + (C_{i\gamma} - C_{i0})S_\gamma}{S_\alpha + S_\beta + S_\gamma} \tag{10}$$

$$\begin{aligned} B_{in} = -\frac{2}{F_n}\cdot\frac{1}{n\pi}\cdot\frac{v}{D_i} \\ \cdot\left\{\sin\left(\frac{n\pi\cdot\frac{S_\alpha}{2}}{S_\alpha + S_\beta + S_\gamma}\right)\cdot(C_{i\beta} - C_{i\alpha}) + \sin\left[\frac{n\pi\cdot\left(\frac{S_\alpha}{2} + S_\beta\right)}{S_\alpha + S_\beta + S_\gamma}\right]\cdot(C_{i\gamma} - C_{i\beta})\right. \\ \left. + \sin\left[\frac{n\pi\cdot\left(\frac{S_\alpha}{2} + S_\beta + S_\gamma\right)}{S_\alpha + S_\beta + S_\gamma}\right]\cdot(C_{i\alpha} - C_{i\gamma})\right\} \end{aligned} \tag{11}$$

$$F_n = \frac{1}{2}\left[1 + \sqrt{1 + \left(\frac{n\pi}{S_\alpha + S_\beta + S_\gamma}\cdot\frac{2D_i}{v}\right)^2}\right] \tag{12}$$

Based on the calculated diffusion solution $C_i(x,z)$ using Eqs. (2) or (9), the constitutional undercooling at the liquid-solid interface before the α phase, $\Delta T_c^\alpha(x, z = 0)$, can be calculated:

$$\Delta T_c^\alpha(x, z = 0) = T_E - T_m^\alpha\big(C_i(x, z = 0)\big) \tag{13}$$

where T_E is the eutectic temperature and T_m^α is the single-phase melting temperature calculated by the Calphad method based on the thermodynamic model of the α phase and the liquid phase. As an example, the T_m-mappings of V_{ss} in the V–Si–B system calculated by the Calphad method based on the thermodynamic model of the V_{ss} phase and the liquid phase created by Pinto da Silva is shown in Fig. 3. Then the average compositional undercooling, ΔT_c, can be calculated:

$$\Delta T_c \text{ (binary eutectic)} = \frac{1}{S_\alpha + S_\beta}\left[\int_0^{S_\alpha} \Delta T_c^{\alpha}(x, z=0)\,\mathrm{d}x + \int_{S_\alpha}^{S_\alpha+S_\beta} \Delta T_c^{\beta}(x, z=0)\,\mathrm{d}x\right] \tag{14}$$

$$\Delta T_c \text{ (ternary eutectic)} = \frac{1}{S_\alpha + S_\beta + S_\gamma}\left[\int_0^{\frac{S_\alpha}{2}} \Delta T_c^{\alpha}(x, z=0)\,\mathrm{d}x + \int_{\frac{S_\alpha}{2}}^{\frac{S_\alpha}{2}+S_\beta} \Delta T_c^{\beta}(x, z=0)\,\mathrm{d}x + \int_{\frac{S_\alpha}{2}+S_\beta}^{\frac{S_\alpha}{2}+S_\beta+S_\gamma} \Delta T_c^{\gamma}(x, z=0)\,\mathrm{d}x + \int_{\frac{S_\alpha}{2}+S_\beta+S_\gamma}^{S_\alpha+S_\beta+S_\gamma} \Delta T_c^{\alpha}(x, z=0)\,\mathrm{d}x\right] \tag{15}$$

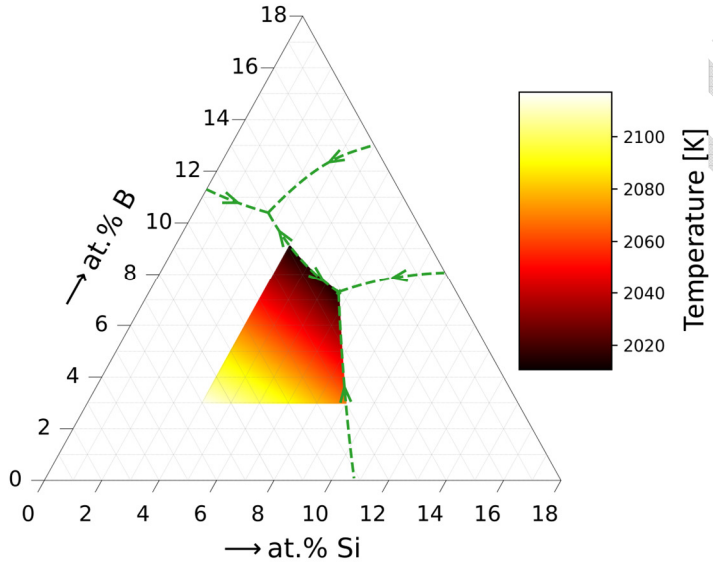

Fig. 3. The T_m-mapping of Vss in the V–Si–B system calculated by the Calphad method based on the thermodynamic model of the Vss phase and the liquid phase created by Pinto da Silva et al. [23]; the green dashed lines represent the liquidus projection calculated by Pinto da Silva et al. [23].

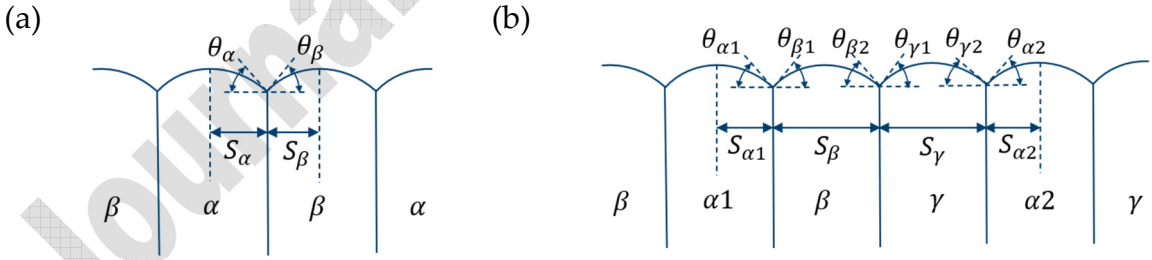

Fig. 4. Schematic illustration of the definition of contact angles, θ, at the three-phase junction for (a) two-phase and (b) three-phase eutectic growth.

The average capillary undercooling, ΔT_σ, can be calculated using the following equations:

$$\Delta T_\sigma \text{ (binary eutectic)} = \frac{2}{\lambda}\left(a_\alpha \sin\theta_\alpha + a_\beta \sin\theta_\beta\right) \tag{16}$$

$$\Delta T_\sigma \text{ (ternary eutectic)} = \frac{1}{\lambda}\cdot\left[a_\alpha(\sin\theta_{\alpha1} + \sin\theta_{\alpha2}) + a_\beta\left(\sin\theta_{\beta1} + \sin\theta_{\beta2}\right) + a_\gamma\left(\sin\theta_{\gamma1} + \sin\theta_{\gamma2}\right)\right] \tag{17}$$

where θ is the contact angle at the three-phase junction shown in Fig. 4 and $a_{\alpha/\beta/\gamma}$ is a constant for each phase given by the Gibbs-Thompson relationship:

$$a_{\alpha/\beta/\gamma} = \frac{T_E}{L_{\alpha/\beta/\gamma}}\sigma^L_{\alpha/\beta/\gamma} \tag{18}$$

where $L_{\alpha/\beta/\gamma}$ is the heat of fusion per unit volume and $\sigma^L_{\alpha/\beta/\gamma}$ is the specific surface free energy of the liquid interface for each phase. In this work, we assume that all contact angles, θ, are equal to 20° [30] and that the Gibbs-Thompson coefficients, $a_{\alpha/\beta/\gamma}$, are equal to the coefficient calculated from the parameters of pure vanadium.

Finally, the total average undercooling, ΔT, can be calculated using the Eq. (1) and the relationship between ΔT, v and λ can be found as follows:

$$\Delta T = K_c \lambda v + \frac{K_\sigma}{\lambda} \tag{19}$$

where K_c corresponds to the constitutional effect, while K_σ corresponds to the capillary effect. K_c needs to be numerically calculated. However, according to Eqs. (16) and (17), K_σ can be determined as follows:

$$K_\sigma \text{ (binary eutectic)} = 2\left(a_\alpha \sin\theta_\alpha + a_\beta \sin\theta_\beta\right) \tag{20}$$

$$K_\sigma \text{ (ternary eutectic)} = a_\alpha(\sin\theta_{\alpha1} + \sin\theta_{\alpha2}) + a_\beta\left(\sin\theta_{\beta1} + \sin\theta_{\beta2}\right) + a_\gamma\left(\sin\theta_{\gamma1} + \sin\theta_{\gamma2}\right) \tag{21}$$

The irregular eutectic growth can occur at a spacing $\lambda = \phi\lambda_{ex}$, where ϕ is the operating constant and λ_{ex} is the spacing corresponding to the minimum ΔT in Eq. (19). Based on this condition, the relationship of ΔT- v can be obtained:

$$\Delta T = \left(\phi + \frac{1}{\phi}\right)\sqrt{K_c K_\sigma}\sqrt{v} = K\sqrt{v} \tag{22}$$

$$K = \left(\phi + \frac{1}{\phi}\right)\sqrt{K_c K_\sigma} \tag{23}$$

Here, it is assumed that the two-phase V_{ss}–V_5SiB_2 and the three-phase V_{ss}–V_3Si–V_5SiB_2 eutectic growth have the same operating constant, ϕ. Then the value of ϕ cannot

influence $\frac{K(V_{ss}\text{-}V_3Si\text{-}V_5SiB_2)}{K(V_{ss}\text{-}V_5SiB_2)}$, the ratio of the K calculated in the two-phase V_{ss}–V_5SiB_2 eutectic growth to the K calculated in the three-phase V_{ss}–V_3Si–V_5SiB_2 eutectic growth:

$$\frac{K(V_{ss}\text{-}V_3Si\text{-}V_5SiB_2)}{K(V_{ss}\text{-}V_5SiB_2)} = \sqrt{\frac{K_c(V_{ss}\text{-}V_3Si\text{-}V_5SiB_2)}{K_c(V_{ss}\text{-}V_5SiB_2)} \cdot \frac{K_\sigma(V_{ss}\text{-}V_3Si\text{-}V_5SiB_2)}{K_\sigma(V_{ss}\text{-}V_5SiB_2)}} \tag{24}$$

This value is used to qualitatively study the competitive solidification behavior between the two eutectic growths depending on the undercooling. Thus, ϕ is assumed as 1 to calculate the absolute value of K:

$$K = 2\sqrt{K_c K_\sigma} \tag{25}$$

The parameters used in this work are listed in Table 2, where the diffusion coefficients of silicon [31] and carbon [32] in liquid iron at 1560 °C were used as an estimate of the diffusion coefficients D_i of silicon and boron in liquid vanadium, respectively, due to the lack of a database. On the assumption that the molar volumes of phases are identical, the phase volume fractions of three-phase eutectic growth can be calculated by:

$$\begin{cases} f_\alpha C_{Si\alpha} + f_\beta C_{Si\beta} + f_\gamma C_{Si\gamma} = C_{Si0} \\ f_\alpha C_{B\alpha} + f_\beta C_{B\beta} + f_\gamma C_{B\gamma} = C_{B0} \\ f_\alpha + f_\beta + f_\gamma = 1 \end{cases} \tag{26}$$

while based on an additional assumption that the initial composition of the two-phase eutectic growth can be adjusted by the solute pile-up of Si at the liquid-solid interface, the phase volume fractions of the two-phase eutectic growth can be calculated by:

$$\begin{cases} f_\alpha C_{B\alpha} + f_\beta C_{B\beta} = C_{B0} \\ f_\alpha + f_\beta = 1 \end{cases} \tag{27}$$

Table 2. The parameters used in this work to calculate K_c and K_σ.

Parameter	Unit	α (V_{ss})– β (V_5SiB_2)	α(V_{ss})– β(V_5SiB_2)– γ(V_3Si)	Ref.
C_0	at.%	V–9Si–6.5B		[this work]
T_E	K	2014		[23]
m		replaced by the T_m-maps of each phase based on the Calphad database from Pinto da Silva et al.		[23]
D_i	$cm^2 \cdot s^{-1}$	4.1 x 10^{-5} (for Si), 1.4 x 10^{-4} (for B)		[31,32]
a	K·cm	1.295 x 10^{-4}		[33,34]
$C_{\alpha(V_{ss})}$	at.%	V–6.24Si		[18]
$C_{\beta(V_5SiB_2)}$	at.%	V–10.51Si–26.98B		[23]
$C_{\gamma(V_3Si)}$	at.%	-	V–20.78Si	[23]
$f_{\alpha(V_{ss})}$	vol.%	76	64	
$f_{\beta(V_5SiB_2)}$	vol.%	24	24	
$f_{\gamma(V_3Si)}$	vol.%	-	12	

3. Results and discussion

3.1. X-ray diffraction

Pawley refinement using the crystal structures of V_{ss} (Im−3m) [35], V_3Si (Pm−3n) [36] and V_5SiB_2 (I4/mcm) [37] can explain the diffraction peaks observed in the samples. After the Pawley refinement, the lattice parameters of each phase can be obtained and are shown in Table 3. Compared to the lattice parameters of the V_{ss}, V_3Si and V_5SiB_2 phases in the alloy V−15Si−7.5B, which was annealed at 1600 °C for 24 h [18], the lattice parameters determined in this work are in reasonably good agreement. Two phases, V_{ss} and V_5SiB_2, were detected by XRD in alloys V−8Si−6.5B (#5) and V−8.5Si−6.5B (#6), while all three phases were detected in the other alloys. However, the measured diffraction peaks of the V_3Si phases in alloy V−8.5Si−7B (#9) are weak as shown in Fig. 5, which indicates the negligible volume fraction of V_3Si phases in alloy V−8.5Si−7B (#9).

Table 3. The calculated lattice parameters of each phase using the Pawley refinement.

Alloy #	Nominal composition [at.%]	V_{ss} (Im−3m)	V_3Si (Pm−3n)	V_5SiB_2 (I4/mcm)	
		a [Å]	a [Å]	a [Å]	c [Å]
1	V−9Si−5.5B	3.024	4.741	5.767	10.743
2	V−9Si−6B	3.023	4.741	5.769	10.744
3	V−9Si−6.5B	3.023	4.740	5.766	10.745
4	V−9Si−7B	3.024	4.740	5.768	10.744
5	V−8Si−6.5B	3.018	-	5.761	10.740
6	V−8.5Si−6.5B	3.016	-	5.767	10.748
7	V−9.5Si−6.5B	3.021	4.740	5.764	10.743
8	V−10Si−6.5B	3.020	4.740	5.765	10.738
9	V−8.5Si−7B	3.017	4.739	5.769	10.751
10	V−9.5Si−6B	3.024	4.742	5.769	10.746
average		3.021	4.740	5.767	10.743
(standard deviation)		(0.003)	(0.001)	(0.002)	(0.005)
V−15Si−7.5B (1600 °C/ 24 h) [18]		3.037	4.746	5.785	10.779

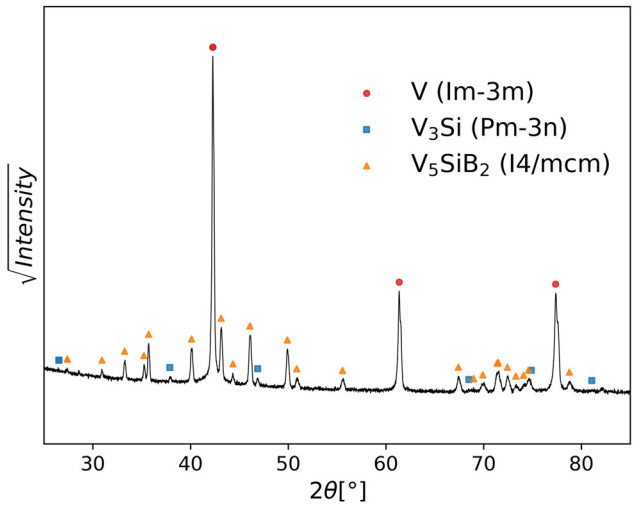

Fig. 5. The XRD pattern of alloy V−8.5Si−7B (#9); the V_3Si phases are negligible due to the weak diffraction peaks of V_3Si phases (marked by blue symbols).

3.2. Determining the ternary V_{ss}–V_3Si–V_5SiB_2 eutectic alloy composition

To determine the ternary V_{ss}–V_3Si–V_5SiB_2 eutectic alloy composition, a three-step approach based on the previous experiments by Hasemann [22] and the alloys V−9Si−5B and V−9Si−7B was performed. First, the Si concentration was kept constant at 9 at.% to study the influence of the B concentration in alloys V−9Si−xB (x = 5.5, 6, 6.5 and 7 at.%). According to the microstructure observations in Fig. 6, the alloy V−9Si−6.5B seems to be closest to the ternary eutectic reaction. In the next step, the Si concentration was varied and the B concentration was fixed to evaluate alloys V−xSi−6.5B (x = 8, 8.5, 9.5 and 10 at.%). Then, the composition of the ternary eutectic reaction in the V-rich region of the V−Si−B system could be determined experimentally. Furthermore, the third set of alloys, V−xSi−(15.5−x)B (x = 8.5 and 9.5 at.%), close to the ternary eutectic reaction, were produced to confirm the determined ternary eutectic composition. Finally, the liquidus projection near the ternary eutectic reaction could be modified.

3.2.1. V−9Si−xB (x = 5.5, 6, 6.5 and 7 at.%)

The three-phase V_{ss}–V_3Si–V_5SiB_2 eutectic microstructures, in which the fibrous V_5SiB_2 phases accompanied by irregularly formed V_3Si phases relatively homogenously distributed in the continuous V_{ss} phases, were obtained in all these 4 alloys as shown in Fig. 6. By contrast, primary dendrites of the V_{ss} phases were observed in alloys V−9Si−5.5B (#1) and V−9Si−6B (#2), while large V_5SiB_2 primary phases were detected in alloy V−9Si−7B (#4). The observation of the two-phase V_{ss}–V_5SiB_2 eutectic microstructure in alloy V−9Si−7B (#4) indicates that the composition of the liquid phase can reach the monovariant V_{ss}–V_5SiB_2 reaction line after the

formation of the primary phase (Fig. 6 (d)). Afterwards, the liquidus composition can change along the monovariant V_{ss}–V_5SiB_2 reaction line until reaching the ternary V_{ss}–V_3Si–V_5SiB_2 eutectic reaction. Most importantly, no primary phases were found in alloy V–9Si–6.5B (#3) (Fig. 6 (c)). Thus, in this set of samples, alloy V–9Si–6.5B (#3) is closest to the ternary eutectic reaction.

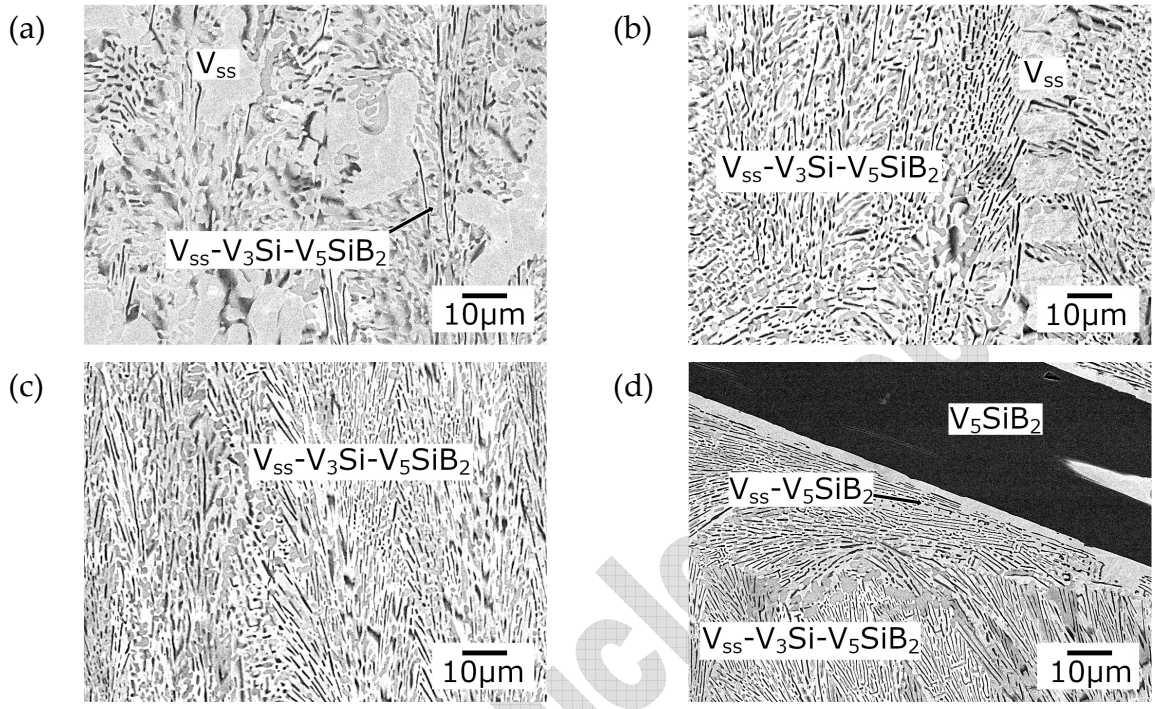

Fig. 6. Microstructures (SEM-BSE) of alloys (a) V–9Si–5.5B (#1), (b) V–9Si–6B (#2), (c) V–9Si–6.5B (#3) and (d) V–9Si–7B (#4); compared to alloys (a) V–9Si–5.5B (#1), (b) V–9Si–6B (#2) and (d) V–9Si–7B (#4), no primary phases but only the ternary V_{ss}–V_3Si–V_5SiB_2 eutectic microstructures were observed in (c) alloy V–9Si–6.5B (#3).

3.2.2. V–xSi–6.5B (x = 8, 8.5, 9.5 and 10 at.%)

In alloy V–8Si–6.5B (#5), the primary lath-shaped V_{ss} phases and the two-phase V_{ss}–V_5SiB_2 eutectics were observed as shown in Fig. 7 (a), which is in agreement with the XRD result in Table 3. Similar to the three-phase V_{ss}–V_3Si–V_5SiB_2 eutectic microstructure, the morphology of the two-phase V_{ss}–V_5SiB_2 eutectic microstructure appears as fibrous V_5SiB_2 phases distributed in V_{ss} major phases. By contrast, alloy V–8.5Si–6.5B (#6) is a two-phase V_{ss}–V_5SiB_2 eutectic alloy without any primary phases (Fig. 7 (b)). This finding indicates that alloy V–8.5Si–6.5B (#6) is closer to the monovariant V_{ss}–V_5SiB_2 line than alloy V–8Si–6.5B (#5).

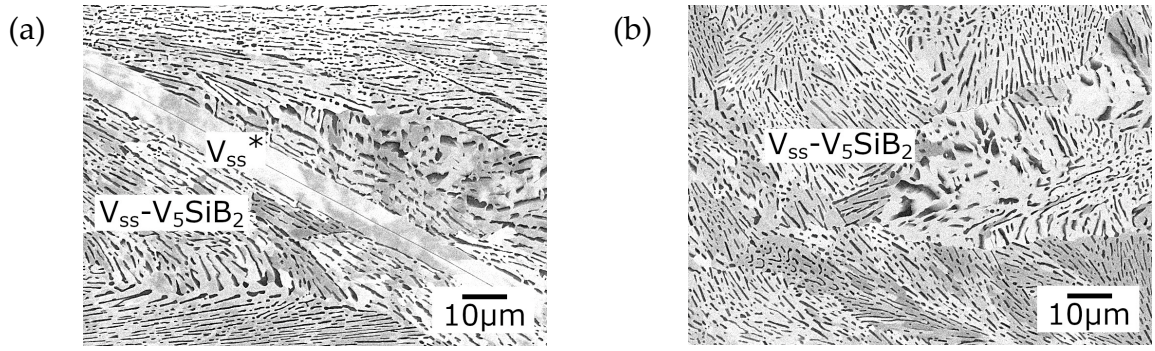

Fig. 7. Microstructures (SEM-BSE) of alloys (a) V−8Si−6.5B (#5) and (b) V−8.5Si−6.5B (#6); primary V_{ss} phases and two-phase V_{ss}–V_5SiB_2 eutectic microstructures were observed in (a) alloy V−8Si−6.5B (#5), while only two-phase V_{ss}–V_5SiB_2 eutectic microstructures were observed in (b) alloy V−8.5Si−6.5B (#6).

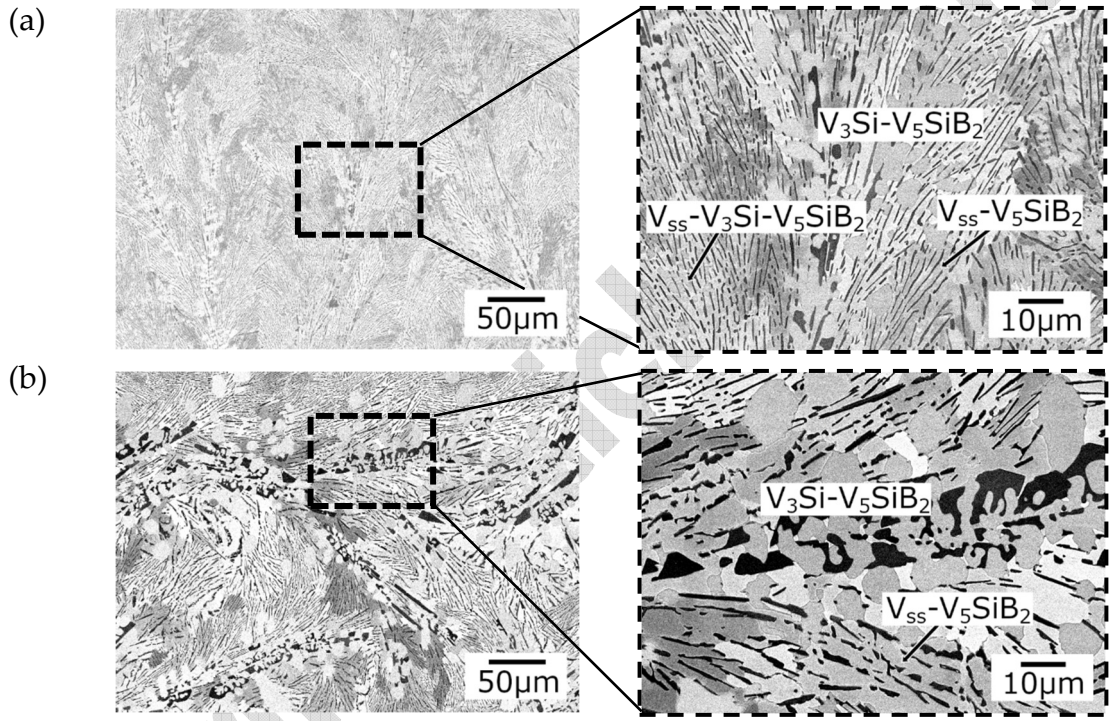

Fig. 8. Microstructures (SEM-BSE) of alloys (a) V−9.5Si−6.5B (#7) and (b) V−10Si−6.5B (#8); two-phase V_3Si–V_5SiB_2 microstructures were observed in both alloys.

As shown in Fig. 8, the two-phase V_3Si–V_5SiB_2 eutectic microstructure can be observed in alloy V−9.5Si−6.5B (#7) and V−10Si−6.5B (#8). Alloy V−9.5Si−6.5B (#7) seems to solidify very close to the V_3Si–V_5SiB_2 monovariant line and consists mostly of the two-phase V_{ss}–V_5SiB_2 and the three-phase V_{ss}–V_3Si–V_5SiB_2 eutectic microstructures (Fig. 8 (a)). The distance from alloy V−9.5Si−6.5B (#7) to the ternary eutectic reaction is less than that from alloy V−10Si−6.5B (#8), which is indicated by a higher volume fraction of V_3Si–V_5SiB_2 in alloy V−10Si−6.5B (#8) (Fig. 8 (b)).

The V_3Si–V_5SiB_2 reaction seems to be strongly affected by undercooling, which at this point makes it difficult to draw any detailed conclusions on the solidification

sequence of those alloys. Thus, the character of the monovariant V_3Si–V_5SiB_2 line (eutectic or possibly weak-peritectic) has not yet been identified.

Based on the experimental results obtained for V–9Si–xB (x = 5.5, 6, 6.5 and 7 at.%) and V–xSi–6.5B (x = 8, 8.5, 9.5 and 10 at.%), the composition of the ternary eutectic alloy was determined at V–9Si–6.5B.

3.2.3. V–xSi–(15.5–x)B (x = 8.5 and 9.5 at.%)

In alloy V–8.5Si–7B (#9) the primary phase V_5SiB_2 and the two-phase V_{ss}–V_5SiB_2 microstructures were obtained (Fig. 9 (a)), while the V_3Si phases were not observed in agreement with the weak diffraction peaks of V_3Si phases in alloy V–8.5Si–7B (#9) as shown in Fig. 5. It suggests that in alloy V–8.5Si–7B (#9) the solidification was completed close to the monovariant V_{ss}–V_5SiB_2 reaction line. By contrast, the microstructure of alloy V–9.5Si–6B (#10) mostly consists of the primary V_3Si phase and the two-phase V_{ss}–V_5SiB_2 eutectic microstructure (Fig. 9 (b)). In addition, a small volume fraction of the three-phase V_{ss}–V_3Si–V_5SiB_2 eutectic microstructure was observed in alloy V–9.5Si–6B (#10) (Fig. 9 (b)).

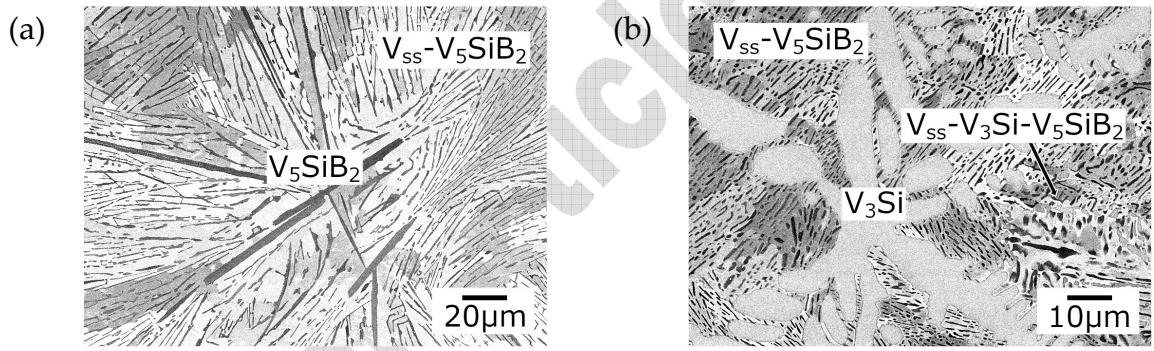

Fig. 9. Microstructures (SEM-BSE) of alloys (a) V–8.5Si–7B (#9) and (b) V–9.5Si–6B (#10); primary V_5SiB_2 phases were observed in (a) V–8.5Si–7B (#9), while primary V_3Si phases were observed in (b) V–9.5Si–6B (#10).

Alloys V–8.5Si–7B (#9) and V–9.5Si–6B (#10) locate close to the ternary eutectic alloy determined in this work, V–9Si–6.5B (#3), at the distance of 0.5 at.% Si and B. The presence of the V_5SiB_2 primary phase in alloy V–8.5Si–7B (#9) and the V_3Si primary phase in alloy V–9.5Si–6B (#10) can again confirm that the ternary eutectic alloy can be found at V–9Si–6.5B.

3.2.4. Modifying the liquidus projection

The liquidus projection close to the V_{ss}–V_3Si–V_5SiB_2 ternary eutectic reaction within the V-rich V–Si–B system has been carefully reinvestigated. Our modifications agree well with the previously published liquidus projection emphasized by Hasemann [22]. Fig. 10 summarizes the present findings and modifications in comparison to the literature data.

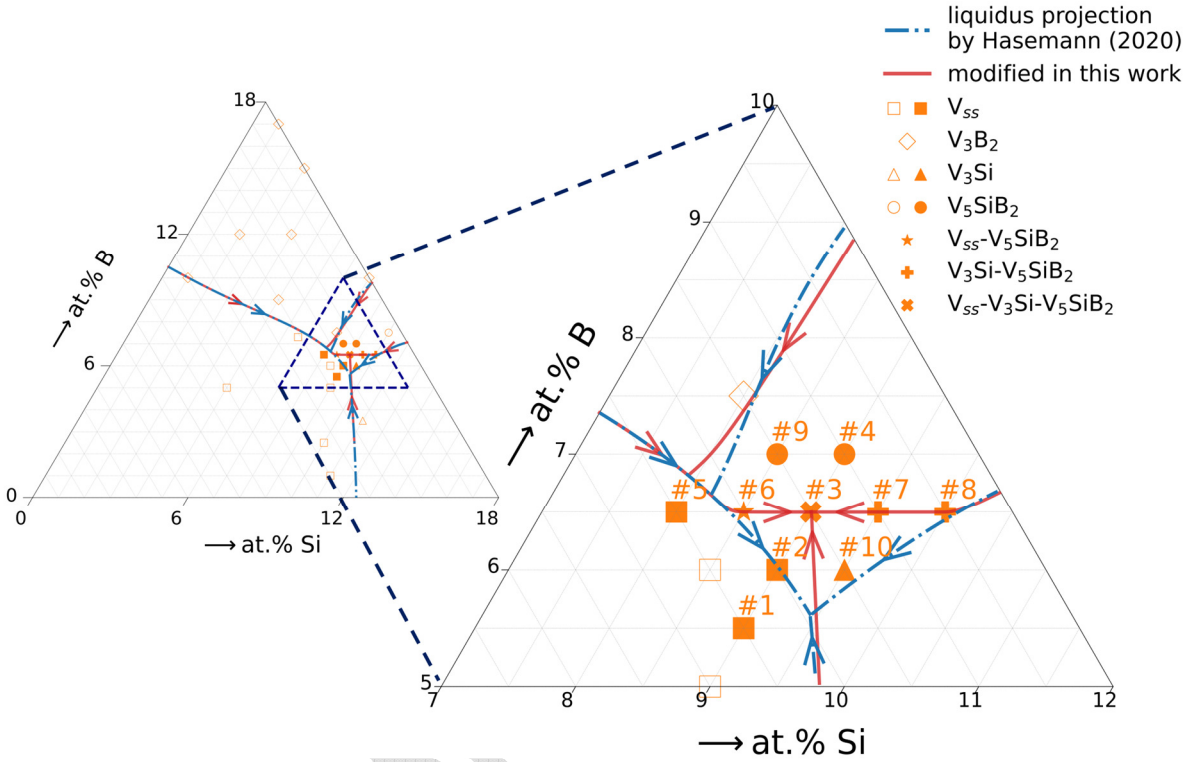

Fig. 10. The liquidus projection near the three-phase V_{ss}–V_3Si–V_5SiB_2 eutectic reaction is modified in the present work based on the liquidus projection measured by Hasemann [22]; the primary phases or the first eutectic microstructures of the alloys investigated are indicated by the filled symbols compared to the results of Hasemann (open symbols).

Firstly, the ternary invariant eutectic reaction $L \leftrightarrow V_{ss} + V_3Si + V_5SiB_2$ (E_t) is moved toward the composition of alloy V–9Si–6.5B (#3) because almost the entire sample is composed of the three-phase V_{ss}–V_3Si–V_5SiB_2 eutectic microstructures (Fig. 6 (c)). This modification can also be confirmed by the observed microstructures of the neighboring alloys at the distance of 0.5 at.% Si and 0.5 at.% B, where microstructures different from the three-phase V_{ss}–V_3Si–V_5SiB_2 microstructures have been found (Fig. 9).

Secondly, the invariant peritectic reaction $L + V_3B_2 \leftrightarrow V_{ss} + V_5SiB_2$ (U) might be slightly shifted to lower Si- and higher B-concentrations, quite close to the composition of alloy V–8Si–6.5B (#5). The alloy solidifies within the V_{ss} primary area but seemingly very close to the two-phase V_{ss}–V_5SiB_2 eutectic valley (Fig. 7 (a)), which indicates its position to be located to the right of the peritectic reaction.

Lastly, both monovariant V_{ss}–V_5SiB_2 and V_3Si–V_5SiB_2 reaction lines near the ternary eutectic reaction seem to be relatively parallel to a B-concentration of around 6.5 at.%. The microstructure of the alloys V–8.5Si–6.5B (#6) (Fig. 7 (b)), V–9.5Si–6.5B (#7) (Fig. 8 (a)) and V–10Si–6.5B (#8) (Fig. 8 (b)) provide the experimental evidence for this assumption. Alloy V–8.5Si–6.5B (#6) is considered as being located very close to the monovariant V_{ss}–V_5SiB_2 reaction line, while alloys V–9.5Si–6.5B (#7) and V–10Si–6.5B (#8) are very close to the monovariant V_3Si–V_5SiB_2 reaction line.

Furthermore, it should be noted that the modified liquidus projection was influenced by the cooling rates in the arc-melting furnace and may slightly vary as compared to the theoretical liquidus projection obtained under equilibrium conditions. However, the difference should be nearly negligible due to the slow cooling rates in the middle region of the arc-melted button.

3.3. Competitive solidification behavior between V_{ss}–V_5SiB_2 and V_{ss}–V_3Si–V_5SiB_2 eutectic growth

In agreement with the results obtained by Hasemann [22] and de Lima et al. [24], the formation of two-phase V_{ss}–V_5SiB_2 microstructures after the formation of two-phase V_3Si–V_5SiB_2 microstructures was observed in the alloys V–9.5Si–6.5B (#7) and V–10Si–6.5B (#8) (Fig. 8). The liquidus projections shown in Fig. 10 cannot explain this phenomenon, because according to the liquidus projections, the three-phase V_{ss}–V_3Si–V_5SiB_2 eutectic formation should be after the two-phase V_3Si–V_5SiB_2 formation. Thus, this phenomenon can be attributed to undercooling effects. To investigate the influence of undercooling effects on the three-phase V_{ss}–V_3Si–V_5SiB_2 eutectic formation, different sections of ternary eutectic alloy V–9Si–6.5B (#3) having experienced different undercoolings were analyzed.

3.3.1. Solidification zones in alloy V–9Si–6.5B (#3)

The longitudinal section of alloy V–9Si–6.5B (#3) along the symmetrical axis of the arc-melted button is shown in Fig. 11 (a), showing a distinct interface between the part near the upper surface of the button and its middle section. Below the interface, columnar growth parallel to the y-axis is can be seen, while the columns above the interface appear distorted towards the sample surface.

In the middle section, a complete three-phase V_{ss}–V_3Si–V_5SiB_2 eutectic microstructure was observed (Fig. 11 (b)). At the sample surfaces, however, a strong morphology change has occurred: the fibrous V_5SiB_2 phases tend to become irregular lamellae, while the irregularly formed V_3Si phases coarsen as shown in Fig. 11 (c) and (d). Even the two-phase V_{ss}–V_5SiB_2 eutectic microstructures can be found in this part

of the sample (Fig. 11 (c)). The cooling rate close to the sample surface is higher than in the middle section of the button. Thus, the three-phase V_{ss}–V_3Si–V_5SiB_2 eutectic formation seems to be more preferable at lower undercoolings, while the two-phase V_{ss}–V_5SiB_2 eutectic microstructures appear to form more preferably at higher undercoolings, as discussed in more detail in the next section.

3.3.2. Calculated result by the eutectic growth theory

The calculated ΔT- v relationships (defined by Eq. (22)) of the two-phase V_{ss}–V_5SiB_2 eutectic growth and the three-phase V_{ss}–V_3Si–V_5SiB_2 eutectic growth are shown in Fig. 12, where $\frac{K(V_{ss}\text{-}V_3Si\text{-}V_5SiB_2)}{K(V_{ss}\text{-}V_5SiB_2)}$ (defined by Eq. (24)) equals to 1.474. This means, the K of the three-phase V_{ss}–V_3Si–V_5SiB_2 eutectic growth is higher than the K of the two-phase V_{ss}–V_5SiB_2 eutectic growth. As a result, at lower undercoolings the three-phase V_{ss}–V_3Si–V_5SiB_2 eutectic growth is preferred because it tends to grow faster than the two-phase V_{ss}–V_5SiB_2 eutectic. By contrast, at higher undercoolings the growth of the two-phase V_{ss}–V_5SiB_2 eutectic becomes preferential. This result agrees well with the observation in the alloy V–9Si–6.5B (#3) (Fig. 11).

Furthermore, the value of $\frac{K_\sigma(V_{ss}\text{-}V_3Si\text{-}V_5SiB_2)}{K_\sigma(V_{ss}\text{-}V_5SiB_2)}$ (K_σ was calculated using Eqs. (20) and (21)), 1.5, is comparable to the value of $\frac{K_c(V_{ss}\text{-}V_3Si\text{-}V_5SiB_2)}{K_c(V_{ss}\text{-}V_5SiB_2)}$ (K_c was numerically determined using Eq. (19)), 1.449. It means that the capillary effect and the constitutional effect contribute similarly to obtaining a higher value of $\frac{K(V_{ss}\text{-}V_3Si\text{-}V_5SiB_2)}{K(V_{ss}\text{-}V_5SiB_2)}$ (defined by Eq. (24)). Thus, although the eutectic growth theory used in this work is based on many assumptions to simplify the complicated eutectic growth, it provides a possible reason for this competitive solidification behavior, i.e. the stronger capillary and constitutional effects of the three-phase V_{ss}–V_3Si–V_5SiB_2 eutectic growth makes it less preferential at higher growth velocities (or undercoolings) compared to the two-phase V_{ss}–V_5SiB_2 eutectic growth due to the additional phase of V_3Si.

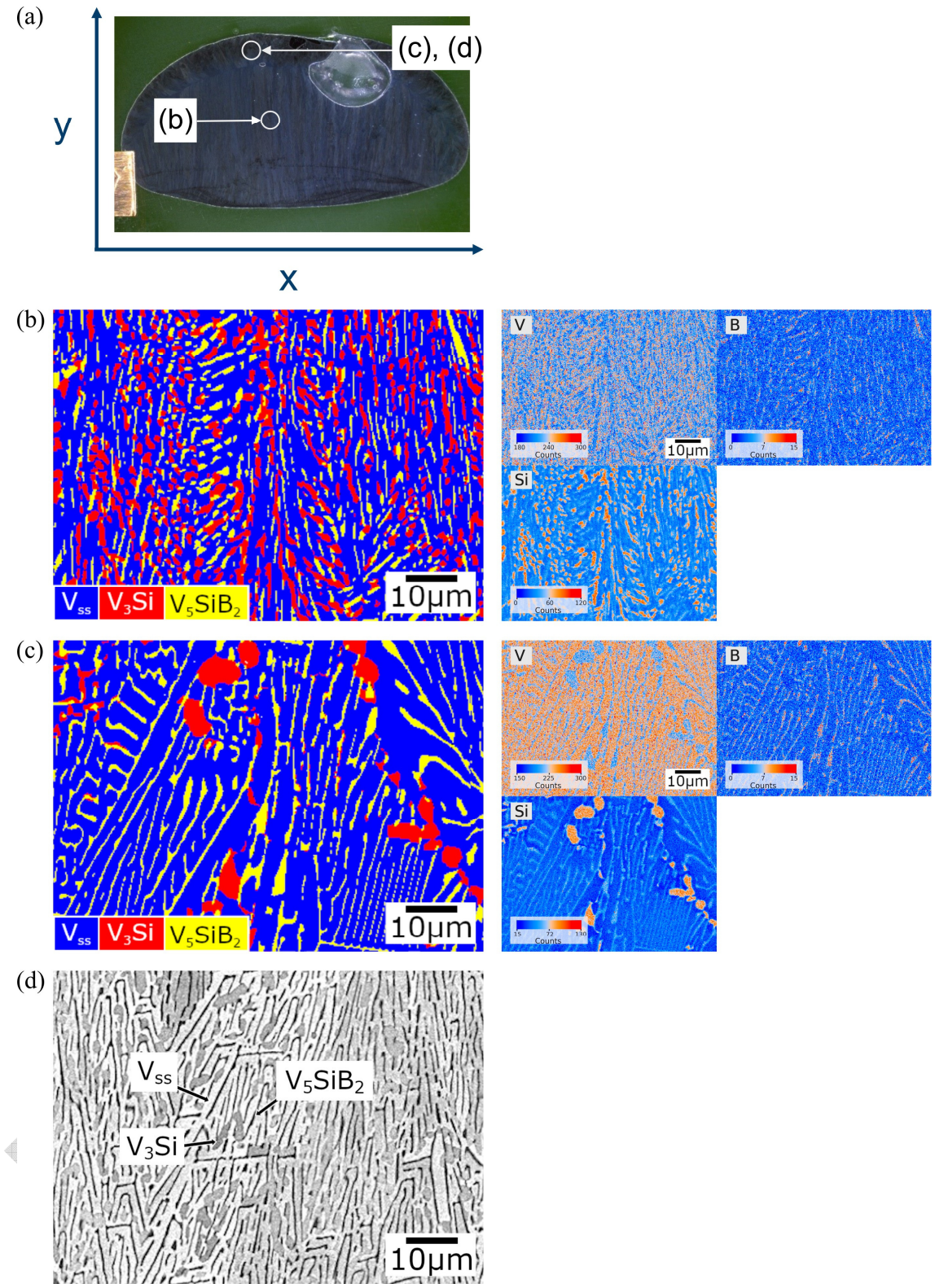

Fig. 11. (a) The longitudinal section (optical microscopy) of the alloy V–9Si–6.5B (#3) along the symmetrical axis of the arc-melted button; the EBSD phase maps confirmed by the EDS mappings (b) in the middle part and (c) close to the sample surface; (d) the SEM-BSE image near the sample surface; compared to the complete three-phase V_{ss}–V_3Si–V_5SiB_2 eutectic microstructures observed (b) in the middle part of the sample, the presence of the two-phase V_{ss}–V_5SiB_2 eutectic microstructures observed (c) in the region close to the sample surface indicates that the two-phase V_{ss}–V_5SiB_2 eutectic growth should be more preferable than the three-phase V_{ss}–V_3Si–V_5SiB_2 eutectic growth at higher undercoolings.

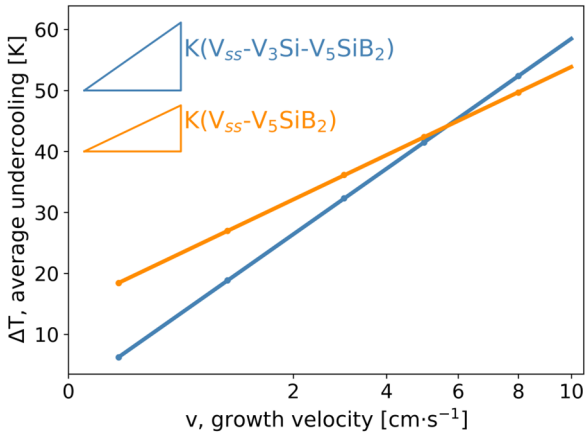

Fig. 12. Comparison of the ΔT- v relationship (defined by Eq. (22)) between the two-phase V_{ss}–V_5SiB_2 eutectic growth and the three-phase V_{ss}–V_3Si–V_5SiB_2 eutectic growth; It can be seen that at lower undercoolings the three-phase V_{ss}–V_3Si–V_5SiB_2 eutectic microstructures form faster, while at higher undercoolings the two-phase V_{ss}–V_5SiB_2 eutectic microstructures form faster.

3.3.3. Explaining the solidification sequence of V_{ss}–V_5SiB_2 after V_3Si–V_5SiB_2

Based on the competitive solidification behavior between the two-phase V_{ss}–V_5SiB_2 and the three-phase V_{ss}–V_3Si–V_5SiB_2 eutectics, the cross section of the three-phase V_{ss}–V_3Si–V_5SiB_2 eutectic coupled zone along the monovariant V_{ss}–V_5SiB_2 and V_3Si–V_5SiB_2 reaction lines near the ternary eutectic reaction is schematically proposed in Fig. 13. Following the approach of Kurz and Fischer [38] to explain the competitive solidification behavior of dendritic and eutectic growth, the three-phase V_{ss}–V_3Si–V_5SiB_2 eutectic coupled zone is skewed to the side of the two-phase V_3Si–V_5SiB_2 reaction line with a higher Si content. The cross section in Fig. 13 can be used to explain the V_{ss}–V_5SiB_2 formation after the V_3Si–V_5SiB_2 formation. During the formation of the V_3Si–V_5SiB_2 microstructure from the liquid phase, the Si-concentration of the liquid decreases along the monovariant V_3Si–V_5SiB_2 line until the liquidus temperature has reached a temperature just below the ternary eutectic reaction. After the formation of the V_3Si–V_5SiB_2 microstructure, the positions of the alloys V–9.5Si–6.5B (#7) and V–10Si–6.5B (#8) will pass through the eutectic reaction and, due to high undercooling, be located in the region of V_{ss}–V_5SiB_2 + V_{ss}–V_3Si–V_5SiB_2 as illustrated in Fig. 13. The region of V_{ss}–V_5SiB_2 + V_{ss}–V_3Si–V_5SiB_2 means that the three-phase V_{ss}–V_3Si–V_5SiB_2 eutectic formation follows after the two-phase V_{ss}–V_5SiB_2 eutectic formation. Thus, this may help to understand the somewhat unexpected solidification sequence of the alloys V–9.5Si–6.5B (#7) and V–10Si–6.5B (#8) according to Fig. 13.

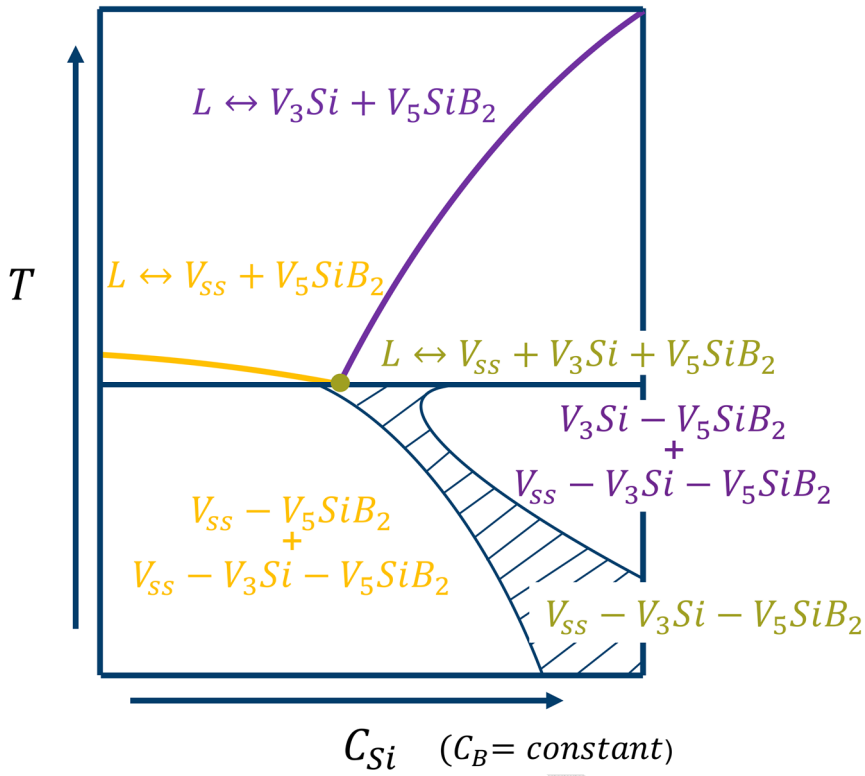

Fig. 13. The schematic illustration of the cross section of the three-phase V_{ss}–V_3Si–V_5SiB_2 eutectic coupled zone along the V_{ss}–V_5SiB_2 and V_3Si–V_5SiB_2 eutectic valleys, where the composition of B is approximated as a constant.

4. Summary

This research work has focused on the three-phase V_{ss}–V_3Si–V_5SiB_2 eutectic formation in the V–Si–B system. Arc-melting was used to identify the ternary eutectic alloy composition. Experimental microstructures of the ternary eutectic alloy at different sample sections were compared with the calculated result of the eutectic growth based on the Jackson-Hunt theory to investigate the competitive solidification behavior between the three-phase V_{ss}–V_3Si–V_5SiB_2 and the two-phase V_{ss}–V_5SiB_2 eutectic growth. Our findings can be summarized as follows:

1. V–9Si–6.5B can be determined as the V_{ss}–V_3Si–V_5SiB_2 ternary eutectic composition. The liquidus projection around this ternary eutectic was modified according to the present results.

2. The three-phase V_{ss}–V_3Si–V_5SiB_2 eutectic formation in alloy V–9Si–6.5B (#3) is preferred at low undercoolings as compared to the two-phase V_{ss}–V_5SiB_2 eutectic formation, while the two-phase V_{ss}–V_5SiB_2 eutectic formation becomes preferred at high undercoolings. The stronger capillary and constitutional effects of the three-phase eutectic compared to the two-phase eutectic are assumed to be the main reason.

3. The three-phase V_{ss}–V_3Si–V_5SiB_2 eutectic coupled zone can be skewed towards the two-phase V_3Si–V_5SiB_2 reaction line and is, therefore, another strong argument for the microstructural evolution involving undercooling effects via arc-melting.

Acknowledgments

This work was supported by the Deutsche Forschungsgemeinschaft (DFG), project number 410338871. The authors would like to thank C. Thomas (PGI–5, FZ Jülich) for providing access to the arc-melter, Dr. E. Wessel (IEK–2, FZ Jülich) and Dr. D. Grüner (IEK–2, FZ Jülich) for their assistance in SEM investigation as well as EBSD and EDS measurements, M. Ziegner (IEK–2, FZ Jülich) for supporting the XRD analysis and K. Wang (IEK–2, FZ Jülich) for helpful discussion about the eutectic growth theory.

References

[1] J.A. Lemberg, R.O. Ritchie, Mo-Si-B Alloys for Ultrahigh-Temperature Structural Applications, Advanced Materials. 24 (2012) 3445–3480. https://doi.org/10.1002/adma.201200764.

[2] P. Jain, K.S. Kumar, Dissolved Si in Mo and its effects on the properties of Mo–Si–B alloys, Scripta Materialia. 62 (2010) 1–4. https://doi.org/10.1016/j.scriptamat.2009.09.008.

[3] F.A. Rioult, S.D. Imhoff, R. Sakidja, J.H. Perepezko, Transient oxidation of Mo–Si–B alloys: Effect of the microstructure size scale, Acta Materialia. 57 (2009) 4600–4613. https://doi.org/10.1016/j.actamat.2009.06.036.

[4] F. Shen, L. Yu, T. Fu, Y. Zhang, H. Wang, K. Cui, J. Wang, S. Hussain, N. Akhtar, Effect of the Al, Cr and B elements on the mechanical properties and oxidation resistance of Nb-Si based alloys: a review, Appl. Phys. A. 127 (2021) 852. https://doi.org/10.1007/s00339-021-05013-7.

[5] F. Shen, Y. Zhang, L. Yu, T. Fu, J. Wang, H. Wang, K. Cui, Microstructure and Oxidation Behavior of Nb-Si-Based Alloys for Ultrahigh Temperature Applications: A Comprehensive Review, Coatings. 11 (2021) 1373. https://doi.org/10.3390/coatings11111373.

[6] S.-N. Jiang, F.-J. Zhou, G.-W. Zhang, X.-O. Yi, C.-W. Yu, X.-J. Wang, W.-F. Rao, Recent progress of vanadium-based alloys for fusion application, Tungsten. 3 (2021) 382–392. https://doi.org/10.1007/s42864-021-00107-4.

[7] X. Guo, W. Zheng, W. An, S. Antonov, L. Li, J. Cormier, Q. Feng, High temperature creep behavior of a cast polycrystalline nickel-based superalloy K465 under thermal cycling conditions, Materialia. 14 (2020) 100913. https://doi.org/10.1016/j.mtla.2020.100913.

[8] M.-H. Tsai, J.-W. Yeh, High-Entropy Alloys: A Critical Review, Materials Research Letters. 2 (2014) 107–123. https://doi.org/10.1080/21663831.2014.912690.

[9] J. Chen, X. Zhou, W. Wang, B. Liu, Y. Lv, W. Yang, D. Xu, Y. Liu, A review on fundamental of high entropy alloys with promising high–temperature properties, Journal of Alloys and Compounds. 760 (2018) 15–30. https://doi.org/10.1016/j.jallcom.2018.05.067.

[10] M. Joele, W.R. Matizamhuka, A Review on the High Temperature Strengthening Mechanisms of High Entropy Superalloys (HESA), Materials. 14 (2021) 5835. https://doi.org/10.3390/ma14195835.

[11] O.N. Senkov, D.B. Miracle, K.J. Chaput, J.-P. Couzinie, Development and exploration of refractory high entropy alloys—A review, J. Mater. Res. 33 (2018) 3092–3128. https://doi.org/10.1557/jmr.2018.153.

[12] Y. Lu, Y. Dong, H. Jiang, Z. Wang, Z. Cao, S. Guo, T. Wang, T. Li, P.K. Liaw, Promising properties and future trend of eutectic high entropy alloys, Scripta Materialia. 187 (2020) 202–209. https://doi.org/10.1016/j.scriptamat.2020.06.022.

[13] M. Wang, Y. Lu, T. Wang, C. Zhang, Z. Cao, T. Li, P.K. Liaw, A novel bulk eutectic high-entropy alloy with outstanding as-cast specific yield strengths at elevated temperatures, Scripta Materialia. 204 (2021) 114132. https://doi.org/10.1016/j.scriptamat.2021.114132.
[14] M. Krüger, High temperature compression strength and oxidation of a V-9Si-13B alloy, Scripta Materialia. 121 (2016) 75–78. https://doi.org/10.1016/j.scriptamat.2016.04.042.
[15] M. Krüger, J. Schmelzer, M. Helmecke, Similarities and Differences in Mechanical Alloying Processes of V-Si-B and Mo-Si-B Powders, Metals. 6 (2016) 241. https://doi.org/10.3390/met6100241.
[16] M. Krüger, V. Bolbut, F. Gang, G. Hasemann, Microstructure Variations and Creep Properties of Novel High Temperature V-Si-B Materials, JOM. 68 (2016) 2811–2816. https://doi.org/10.1007/s11837-016-2096-6.
[17] M. Krüger, B. Köppe-Grabow, Process-Oriented Microstructure Evolution of V_{ss}-V_3Si-V_5SiB_2 Materials, Practical Metallography. 54 (2017) 293–307. https://doi.org/10.3139/147.110456.
[18] C.A. Nunes, B.B. de Lima, G.C. Coelho, P.A. Suzuki, Isothermal Section of the V-Si-B System at 1600 °C in the V-VSi_2-VB Region, Journal of Phase Equilibria and Diffusion. 30 (2009) 345–350. https://doi.org/10.1007/s11669-009-9533-y.
[19] R.C. Reed, T. Tao, N. Warnken, Alloys-By-Design: Application to nickel-based single crystal superalloys, Acta Materialia. 57 (2009) 5898–5913. https://doi.org/10.1016/j.actamat.2009.08.018.
[20] C.H. Zenk, S. Neumeier, N.M. Engl, S.G. Fries, O. Dolotko, M. Weiser, S. Virtanen, M. Göken, Intermediate Co/Ni-base model superalloys — Thermophysical properties, creep and oxidation, Scripta Materialia. 112 (2016) 83–86. https://doi.org/10.1016/j.scriptamat.2015.09.018.
[21] K. Natesan, M. Uz, Oxidation performance of V-Cr-Ti alloys, Fusion Engineering and Design. 51–52 (2000) 145–152. https://doi.org/10.1016/S0920-3796(00)00308-2.
[22] G. Hasemann, Experimental study of the liquidus surface in the V-rich portion of the V-Si-B system, Journal of Alloys and Compounds. 824 (2020) 153843. https://doi.org/10.1016/j.jallcom.2020.153843.
[23] A.A.A. Pinto da Silva, N. Chaia, F. Ferreira, G. Carvalho Coelho, J.-M. Fiorani, N. David, M. Vilasi, C.A. Nunes, Thermodynamic modeling of the V-Si-B system, Calphad. 59 (2017) 199–206. https://doi.org/10.1016/j.calphad.2017.10.001.
[24] B.B. de Lima, C.A. Nunes, G.C. Coelho, PROJEÇÃO LIQUIDUS DO SISTEMA V-Si-B NA REGIÃO RICA EM VANÁDIO, Congresso Brasileiro de Engenharia e Ciência Dos Materiais. (2002) 2640–2646.
[25] K.A. Jackson, J.D. Hunt, Lamellar and Rod Eutectic Growth, in: Dynamics of Curved Fronts, Elsevier, 1988: pp. 363–376. https://doi.org/10.1016/B978-0-08-092523-3.50040-X.
[26] B.H. Toby, R.B. Von Dreele, GSAS-II: the genesis of a modern open-source all purpose crystallography software package, Journal of Applied Crystallography. 46 (2013) 544–549. https://doi.org/10.1107/S0021889813003531.
[27] G.S. Pawley, Unit-cell refinement from powder diffraction scans, Journal of Applied Crystallography. 14 (1981) 357–361. https://doi.org/10.1107/S0021889881009618.
[28] P. Magnin, W. Kurz, An analytical model of irregular eutectic growth and its application to Fe-C, Acta Metallurgica. 35 (1987) 1119–1128. https://doi.org/10.1016/0001-6160(87)90059-9.
[29] R. Trivedi, P. Magnin, W. Kurz, Theory of eutectic growth under rapid solidification conditions, Acta Metallurgica. 35 (1987) 971–980. https://doi.org/10.1016/0001-6160(87)90176-3.
[30] T. Himemiya, T. Umeda, Three-Phase Planar Eutectic Growth Models for a Ternary Eutectic System, Materials Transactions, JIM. 40 (1999) 665–674. https://doi.org/10.2320/matertrans1989.40.665.
[31] F.P. Calderon, N. Sano, Y. Matsushita, Diffusion of managenese and silicon in liquid iron over the whole range of composition, Metall and Materi Trans B. 2 (1971) 3325–3332. https://doi.org/10.1007/BF02811613.
[32] D. Goldberg, G.R. Belton, The diffusion of carbon in iron-carbon alloys at 1560°C, Metall Mater Trans B. 5 (1974) 1643–1648. https://doi.org/10.1007/BF02646337.
[33] J.W. Arblaster, Thermodynamic Properties of Vanadium, J. Phase Equilib. Diffus. 38 (2017) 51–64.

https://doi.org/10.1007/s11669-016-0514-7.

[34] F. Aqra, A. Ayyad, Surface tension (γLV), surface energy (γSV) and crystal-melt interfacial energy (γSL) of metals, Current Applied Physics. 12 (2012) 31–35. https://doi.org/10.1016/j.cap.2011.04.020.

[35] P. Karen, E. Suard, F. Fauth, Crystal Structure of Stoichiometric $YBa_2Fe_3O_8$, Inorg. Chem. 44 (2005) 8170–8172. https://doi.org/10.1021/ic048746b.

[36] J.-L. Staudenmann, The electron charge distribution in V_3Si, Solid State Communications. 26 (1978) 461–468. https://doi.org/10.1016/0038-1098(78)91290-5.

[37] H. Kudielka, H. Nowotny, G. Findeisen, Untersuchungen in den Systemen: V-B, Nb-B, V-B-Si und Ta-B-Si, Monatshefte für Chemie. 88 (1958) 1048–1055. https://doi.org/10.1007/BF00906084.

[38] W. Kurz, D.J. Fisher, Fundamentals of solidification, 3. rev. ed., reprinted, Trans Tech Publ, Aedermannsdorf, 1992.